

# A Raman lidar at La Reunion (20.8° S, 55.5° E) for monitoring water vapor and cirrus distributions in the subtropical upper troposphere: preliminary analyses and description of a future system

Christophe Hoareau, Philippe Keckhut, Jean-Luc Baray, Laurent Robert, Yann Courcoux, Jacques Porteneuve, H. Vömel, Béatrice Morel

▶ **To cite this version:**

Christophe Hoareau, Philippe Keckhut, Jean-Luc Baray, Laurent Robert, Yann Courcoux, et al.. A Raman lidar at La Reunion (20.8° S, 55.5° E) for monitoring water vapor and cirrus distributions in the subtropical upper troposphere: preliminary analyses and description of a future system. Atmospheric Measurement Techniques, 2012, 5 (6), pp.1333-1348. 10.5194/amt-5-1333-2012 . hal-00635877

**HAL Id: hal-00635877**
**https://hal.science/hal-00635877**

Submitted on 16 Jun 2017

**HAL** is a multi-disciplinary open access archive for the deposit and dissemination of scientific research documents, whether they are published or not. The documents may come from teaching and research institutions in France or abroad, or from public or private research centers.

L'archive ouverte pluridisciplinaire **HAL**, est destinée au dépôt et à la diffusion de documents scientifiques de niveau recherche, publiés ou non, émanant des établissements d'enseignement et de recherche français ou étrangers, des laboratoires publics ou privés.

Atmos. Meas. Tech., 5, 1333–1348, 2012
www.atmos-meas-tech.net/5/1333/2012/
doi:10.5194/amt-5-1333-2012
© Author(s) 2012. CC Attribution 3.0 License.



Atmospheric Measurement Techniques

# A Raman lidar at La Reunion (20.8° S, 55.5° E) for monitoring water vapour and cirrus distributions in the subtropical upper troposphere: preliminary analyses and description of a future system

**C. Hoareau[1,**], P. Keckhut[1], J.-L. Baray[2,4], L. Robert[2], Y. Courcoux[4], J. Porteneuve[1], H. Vömel[3], and B. Morel[2,*]**

[1]LATMOS, UMR8190, INSU-CNRS – UVSQ, UPMC, 11 Boulevard d'Alembert, 78820 Guyancourt, France
[2]LACy, UMR8105, 15 avenue René Cassin, BP 7151, 97715 St-Denis Cedex 09, La Réunion, France
[3]Meteorological Observatory Lindenberg, Deutscher Wetterdienst, Am Observatorium 12, 15848 Lindenberg, Germany
[4]OSU Réunion, UMS3365, 15 avenue René Cassin, BP 7151, 97715 St-Denis Cedex 09, La Réunion, France
[*]now at: LE2P, 15 avenue René Cassin, BP 7151, 97715 St-Denis Cedex 09, La Réunion, France
[**]now at: LMD, UMR8539, INSU-CNRS, UPMC, Ecole Polytechnique, 91128 Palaiseau Cedex, France

*Correspondence to:* C. Hoareau (christophe.hoareau@lmd.polytechnique.fr)

Received: 7 October 2011 – Published in Atmos. Meas. Tech. Discuss.: 25 October 2011
Revised: 28 April 2012 – Accepted: 18 May 2012 – Published: 13 June 2012

**Abstract.** A ground-based Rayleigh lidar has provided continuous observations of tropospheric water vapour profiles and cirrus cloud using a preliminary Raman channels setup on an existing Rayleigh lidar above La Reunion over the period 2002–2005. With this instrument, we performed a first measurement campaign of 350 independent water vapour profiles. A statistical study of the distribution of water vapour profiles is presented and some investigations concerning the calibration are discussed. Analysis regarding the cirrus clouds is presented and a classification has been performed showing 3 distinct classes. Based on these results, the characteristics and the design of a future lidar system, to be implemented at the new Reunion Island altitude observatory (2200 m) for long-term monitoring, is presented and numerical simulations of system performance have been realised to compare both instruments.

## 1 Introduction

Water vapour has long been recognised as one of the most important trace gases in the atmosphere. The measurements of water vapour profiles are important for understanding and forecasting of the moisture convection and horizontal transport. Water vapour plays also a crucial role in many aspects of the Upper Troposphere and Lower Stratosphere (UTLS). It contributes strongly to the radiative balance of the atmosphere and plays an important role in global climate (Forster and Shine, 2002; Kley et al., 2000). Measuring accurately the water vapour concentration in the UTLS region is a difficult task given its very low concentration and its large variability. Water vapour can be considered for the study of tropical and sub-tropical atmospheric dynamical phenomena and their roles in the local and global circulations and in climate changes through vertical and horizontal transport, in particular, through tropical and sub-tropical Stratosphere Troposphere Exchanges (STE). However, condensation into ice during cirrus formation redistributes water downward through subsidence effects of heavy particles. Upper tropospheric water vapour in the tropics and subtropics is strongly influenced by the Hadley Cell and the Walker circulation (Kley et al., 2000). Widening of the tropics may also lead to changes in the distribution of climatically important trace gases in the stratosphere. The Brewer-Dobson circulation moves air upwards from the troposphere into the stratosphere in the tropics. If the area over which this upwelling occurs increases, transport of water vapour into the stratosphere might be enhanced. This could lead to an enhanced greenhouse house effect, including tropospheric warming and stratospheric cooling and reduced ozone (Seidel et al.,

2008; Forster and Shine, 2002; Kirk-Davidoff et al., 1999). Tropospheric and stratospheric water vapour has been measured over the past decades by a large number of instruments with different characteristics and limitations (Kley et al., 2000). Water vapour measurements using the Raman lidar are not new (Cooney, 1970; Ferrare et al., 1995; Whiteman et al., 1992). This technique is one of the only ones which enables the probing of the upper troposphere and tropopause region. Moreover, the possibility of acquiring an elastic signal simultaneously with water vapour Raman signals is of great interest for providing information about ice crystal occurrence. Capabilities have been successively improved with larger commercial laser power availability (Sakai et al., 2007; Sherlock et al., 1999a; Leblanc et al., 2008; Whiteman et al., 2010). Some preliminary Raman channels have been setup on an existing Rayleigh lidar to perform first investigations and capabilities evaluations to measure water vapour in the upper troposphere and to design a future specific instrument. In this publication, a brief description of data retrievals and the design of the instrument have been described in Sects. 2 and 3. Data processing, regarding calibration and validation aspect, is exposed in Sect. 4. A statistical study of subtropical water vapour and scattering ratio profiles from Raman lidar is presented in Sect. 5 and the description of the design of a new specific Raman lidar to be implemented at the Maïdo altitude station is presented in Sect. 6.

## 2 Water vapour and cirrus cloud optical depth calculation from Raman lidar

### 2.1 Water vapour mixing ratio

The ratio of the mass of water vapour to the mass of dry air in a given volume, known as the water vapour mixing ratio, is a convenient measure of the amount of water vapour in the atmosphere. As atmospheric nitrogen forms a constant proportion of dry air (∼78 %) in the lower atmosphere, normalizing the $H_2O$ Raman return with the $N_2$ Raman profile allows mixing ratio to be derived. Accounting for the atmospheric differential transmission $\Gamma(z)$ and the calibration coefficient $C$, it can be calculated using the following expression (Sherlock et al., 1999a; Whiteman et al., 1992):

$$q(z) = C\Gamma(z)\frac{S_{H_2O}(z)}{S_{N_2}(z)} \quad (1)$$

The calibration aspect is an important issue to insure an accurate monitoring. Various approaches have been tested to calibrate the water vapour measurements of a Raman lidar system. However, calibration issues are still pending and debated (Whiteman et al., 2011a; Leblanc and McDermid, 2008). Though an absolute calibration of the entire lidar system is theoretically possible (Vaughan et al., 1988; Sherlock et al., 1999b; Venable et al., 2011), the signal ratio is usually scaled to various external water vapour measurements (radiosonde, microwave radiometer, Global Positioning System (GPS),. . . ) in order to deduce water vapour mixing ratio. Calibration coefficients determined from nearby radiosondes are commonly used, but their reliability for long-term continuity is questionable (Soden and Lanzante, 1996) and independent techniques have been investigated (Sherlock et al., 1999a, b). The Network for the Detection of Atmospheric Composition Change (NDACC) has recently established long-term monitoring of water vapour using Raman lidar as one of its core objectives (Leblanc et al., 2008). One of the principal needs for developing a long-term dataset for monitoring atmospheric trends is a calibration that varies randomly around some mean value and does not involve step jumps of unknown magnitude or significant drifts (Whiteman et al., 2011a). For this reason, it is essential to carefully investigate any calibration techniques developed for ensuring stable, long-term calibrations even if a greater tolerance for random uncertainty budgets in the time series for upper troposphere trend detection relaxes the need for calibration accuracy of Raman lidar, which makes the challenge of calibration perhaps easier to meet (Whiteman et al., 2011b).

### 2.2 Cirrus cloud optical depth retrieval

The optical thickness of cirrus is calculated in accordance with the aerosol Scattering Ratio profile (SR) which is defined as the ratio of the total (molecular and particle) backscatter coefficient divided by the molecular backscatter coefficient. Because molecular backscattering can be estimated by a dry air density profile, it can further be retrieved from the nitrogen signal, so SR can be derived from the ratio of the power in the Rayleigh-Mie and Raman vibrational $N_2$ channels (Ferrare et al., 2001). However, even if the Raman technique can be utilised to retrieve the extinction, in our case, the nitrogen signal backscattered is too noisy in many measurements for an accurate determination of optical depth. So we choose to calculate the optical thickness of cirrus, $\tau_{\text{cirrus}}$, from a method similar to that described by Goldfarb et al. (2001), where $\tau_{\text{cirrus}}$ can be expressed by the following expression:

$$\tau_{\text{cirrus}} = (\text{LR})\sigma_{\text{rayleigh}} \int_{Z_{\min}}^{Z_{\max}} n_{\text{air}}(z)(\text{SR}(z) - 1)\text{d}z \quad (2)$$

Where $\beta_{\text{rayleigh}} = \sigma_{\text{rayleigh}} n_{\text{air}}(z)$ and the air density number $n_{\text{air}}(z)$ are calculated by the Mass Spectrometer Incoherent Scatter-Extended-1990 (MSISE-90) atmospheric model and $\sigma_{\text{rayleigh}}$ (532 nm) = $5.7 \times 10^{-32}\,\text{m}^2\,\text{sr}^{-1}$. To be able to retrieve with the same confidence all cases including thin or thick clouds, a lidar ratio (LR) of 18.2 sr (Platt and Dilley, 1984) is used. Over the year, some different values of mean LR have been retrieved; however, analysis based on Raman lidar measurements yield LR values in quite good agreement with this value (Reichardt et al., 2002; Cadet et al., 2005). Furthermore, subdivision by cirrus generating mechanism (e.g., Sect. 5.4) seems to not influence significantly the

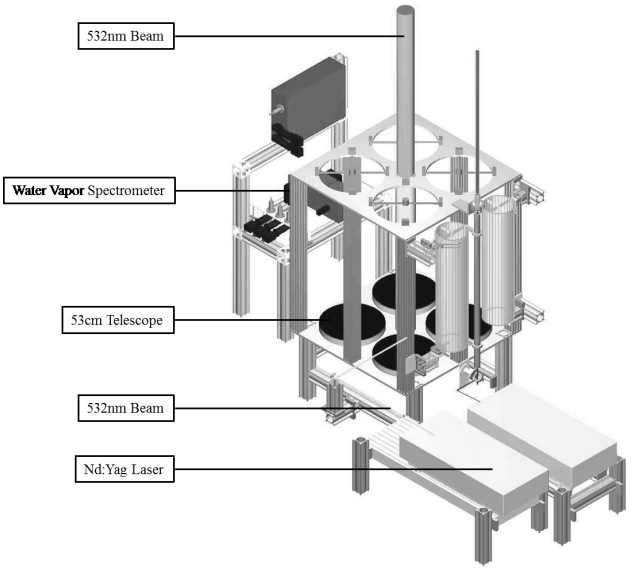



**Fig. 1.** Representation of the lidar instrument at Reunion Island university during the 2002–2005 period.

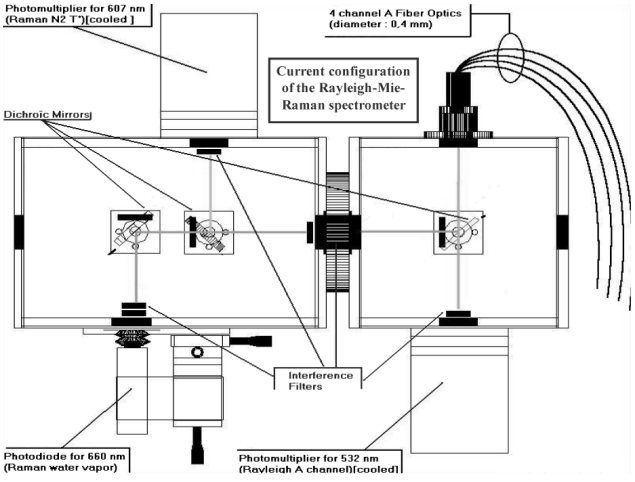



**Fig. 2.** Schematic representation of the current configuration of the Rayleigh-Mie-Raman spectrometer of the preliminary lidar system.

layer mean LR consistent with the assumption in this study (Whiteman et al., 2004).

## 3 Technical description of the instrument

The Raman water vapour lidar system deployed at La Reunion is an upgrade of the receiving optics of the existing Rayleigh-Mie lidar system which operates on a routine basis at night, except in presence of low cloud at the Observatoire de Physique de l'Atmosphère de La Réunion (OPAR), hosted by Reunion Island university at 80 m above sea level (ASL) (Baray et al., 2006). Regular water vapour measurements have been realised with this configuration over the period 2002–2005. This long campaign allowed us to perform a preliminary study of water vapour monitoring capabilities and to evaluate the needs regarding a more specific lidar system to be implemented at the future altitude facility at Piton Maïdo mount (2200 m a.s.l.). During this period, about a hundred acquisition nights have been acquired using the Raman channels.

The Raman lidar system is based on a Nd:Yag laser source with a repetition rate of 30 Hz and the second harmonic is used. The pulse energy at 532.1 nm is 800 mJ/pulse (9 ns pulse length). The radiation backscattered by the atmosphere is collected by optical fibres mounted on the focal plane of a 4-telescope mosaic (0.53 m diameter each) of Newtonian type with a field-of-view of 1mrad and transferred to the optical ensemble. A schematic representation of the Rayleigh lidar instrument is given in Fig. 1. In this ensemble, the received wavelengths are spectrally separated through a set of dichroic beam splitters, mirrors and bandwidth pass-band interference filters (BPIF) as shown in Fig. 2. The beam reflected toward this ensemble is, firstly, filtered by a high-pass interference filter specially designed to reject the remaining 532 nm component with a rejection ratio between the transmitted and incident energy at 532 nm of $10^{-5}$: this filter has a maximum transmission of 91.5 % at 607 nm and of 89.2 % at 660 nm. The filtered beam is then split by another dichroic beam splitter that reflects its 607 nm component toward the photomultiplier (PMT) of the Raman $N_2$ channel and transmits its 660 nm component toward a metallic mirror that finally reflects the 660 nm component toward an avalanche photodiode (APD) which is the detector of the Raman $H_2O$ channel. A BPIF with a maximum transmission of 57 % at 607 nm and a full width at half maximum (FWHM) of 1nm is placed in front of the $N_2$ PMT and aims notably to reject the residual 532 nm component which passed through the high-pass interference filter. A focusing lens with a focal length of 50 mm is placed after this filter to focus the Raman 607 nm component onto the photocathode of the $N_2$ PMT. Two three-cavity interference filters are used on the $H_2O$ channel to ensure that the Rayleigh-Mie contribution and Raman contributions from $N_2$ and $O_2$ are less than 0.1 % of the water vapour signal in all measurement conditions. The BPIFs placed in front of the $H_2O$ photodiode have a maximum transmission of 80 % and 57 % at 660 nm and, respectively, a FWHM of 5nm and 1nm. The detector used for the Raman $N_2$ channel is a multi-alkali 9-stages Hamamatsu R1477 circular-cage PMT that is cooled down to a temperature of about $-20\,^{\circ}$C through a Hamamatsu Peltier cooling mechanism. When cooled, this PMT has a low dark current (<5 counts per second). Here, PMT cooling permits the reduction of the background noise (sky background and detector noise) by a factor $\sim$2 compared to the background noise obtained by the use of PMT with a typical dark count rate of $\sim 100\,\mathrm{cps\,s^{-1}}$. Although the skylight background is much larger than detector noise for daytime measurement,

reduction of both noise sources for system operating at night must be considered. This PMT has a quantum efficiency of about 12 % at 607 nm and its typical voltage operation is less than 900 V to limit the signal-induced bias associated with the PMT response to an intense luminous pulse (Acharya et al., 2004). PMT pulses are typically 8ns in duration and the maximum count rate for a Poisson signal with exponentially distributed inter-arrival times is 45 MHz. An avalanche photodiode has been used for the Raman $H_2O$ channel because of the better quantum detection efficiencies of these detectors at visible wavelengths compared to classical PMTs. In addition, the technology of photodiodes generally offers better overall detection efficiencies in the red and near-infrared parts of the spectrum. The APD model used for the $H_2O$ channel is an EG & G SPCM AQ-232 photodiode. This photodiode is uncooled, but has a very low temperature dependence of its characteristics. Its quantum efficiency is about 35 % at 660 nm. Contrary to PMTs, it is not possible to set the supply voltage of the photodiode and it must be noticed that the output of this detector is a standardized logic pulse: a 2 V logic pulse with a temporal length of about 40 ns corresponding to each detected photon. The main drawback of this photodiode is its detection surface which is a disc with a diameter of 480 µm: this entails an important sensitivity of the $H_2O$ channel to optical misalignment and also does not ease the alignments of the photodiode. It is essential to use very-low-noise detectors for detecting the very weak water vapour returns. The maximum count rate for a Poisson signal with exponentially distributed inter-arrival times is 10 MHz.

## 4 Description of data processing

### 4.1 Methodology and validation

Raman lidar profiles of water vapour mixing ratio are determined by taking the ratio of Raman backscatter by water vapour to Raman backscatter by one of the well mixed gases such as nitrogen (e.g., Sect. 2.1). In the middle and upper troposphere, aerosols densities are generally small and ice clouds do not exhibit large wavelength attenuation dependence. Though it can be estimated with additional channels (Faduilhe et al., 2005), it has been proved that the relative transmission of the Raman returns, at 607 nm ($N_2$) and 660 nm ($H_2O$), corresponds to a 0–5 % overestimation in extreme aerosol loading conditions. This systematic bias introduced in water vapour profiles has been corrected from molecular attenuation and absorption by ozone coefficients of the US Standard Atmosphere. Due to the large bandwidth of the interferential filter (1 nm), no temperature dependence corrections have been applied. Investigations concerning the temperature dependence performed by Sherlock et al. (1999b) have shown that water vapour mixing ratio may be overestimated by ∼2 % in the upper troposphere. Although these investigations have been realised for the lidar implanted at the Observatory of Haute-Provence, the configuration of the optical ensemble and the optical component used are identical for both lidar which involved similar results. This temperature dependence is very weak and negligible for practical purposes compared with random errors.

The water vapour mixing ratio profiles are obtained by averaging pre-accumulated lidar signals (typically 2 min) over an a priori period of quasi-stationary conditions regarding statistical variability. Assuming stationary atmospheric conditions, the backscattered photons hit the counter independently and the counting follows a Poisson process. Thus, from a statistical point-of-view, the mixing ratio derived from the signal averaging is equivalent to the averaging of the individual mixing ratio profiles. Because the photon-counting process is described by a Poisson statistics, long enough sampling periods provide a better statistical estimator of the water vapour mixing ratio. However, if the sampling period is too long, information about the variability is lost. To achieve a reasonable compromise between accuracy and atmospheric variability, the applied method consists of adjusting the integration time with the discontinuity of the flow sounded. The identification of discontinuities in the time series is based on the test of non-stationarity of the series due to a change in dispersion in the $H_2O/N_2$ ratio time series as described by Hoareau et al. (2009). Under the assumption that two successive profiles give a variability of the same order, they can be considered as independent measurements. In clear sky condition, this Raman lidar system allows the performing of measurements of water vapour mixing ratio profiles that extend up to the tropopause region in nighttime conditions.

In 2005–2006, a campaign of CFH (Cryogenic Frost point Hygrometer) measurements was organised at Reunion Island. The CFH is sensor carried under a balloon which measures water vapour continuously between the surface and the lower stratosphere (Vömel et al., 2007). It is based on the chilled mirror principle and measures the temperature of a mirror carrying a thin dew or frost layer, which is maintained in equilibrium with the ambient water vapour. The optical phase sensitive detector measures the bulk reflectivity of the mirror and the microprocessor feedback controller regulates the mirror temperature such that the bulk reflectivity and, hence, the condensate layer remain constant. Under this condition the condensate layer on the mirror is in thermal equilibrium with the vapour phase of the air passing over the mirror. The mirror temperature is then equal to the ambient dew point or frost point temperature and the water vapour mixing ratio and relative humidity can be calculated from this observation using a variation of the Clausius Clapeyron equation. Like many chilled mirror instruments, CFH does not need to be calibrated for water vapour and can be considered as an absolute reference for water vapour measurements. The total uncertainty in frost point is better than 0.5 K throughout the entire profile, which means a mixing ratio uncertainty of about 4 % in the lower tropical troposphere and about 10 % in the middle stratosphere and tropical tropopause (Vömel et

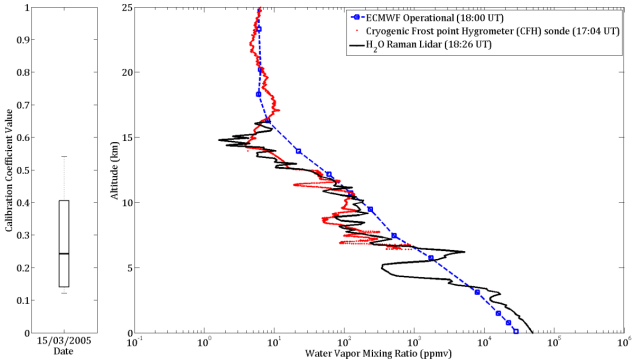



**Fig. 3.** Intercomparison between $H_2O$ Raman lidar (black line), Cryogenic Frost point Hygrometer (CFH) sonde (red dots) and ECMWF operational analysis (blue line) on 15 March 2005. The calibration coefficient and its error are shown on the left. Calibration has been realised using ECMWF Operational data before comparison with CFH.

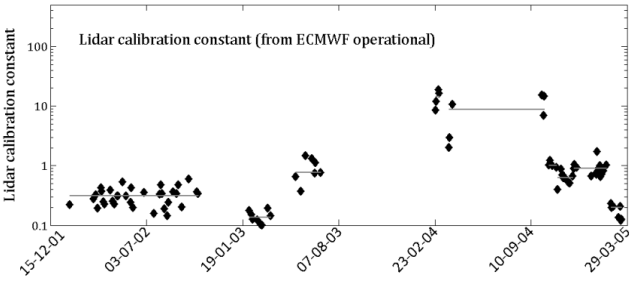



**Fig. 4.** Time evolution of the actual lidar calibration constant over the period 2002–2005. The horizontal grey lines represent the median of these coefficients.

al., 2007). In Fig. 3, an intercomparison between $H_2O$ Raman lidar, (CFH) sonde and the European Center for Medium-Range Weather Forecast (ECMWF) operational is shown. Calibration has been realised here using ECMWF Operational data (e.g., Sect. 4.2). The water vapour mixing ratio profile obtained during the descent of the CFH sonde is used here to validate the lidar profile in the upper troposphere. The integration time of the water vapour mixing ratio profile is ∼50 min, and the random error of the profile is inferior to 1 % up to ∼5 km, reached 10 % from ∼12 km and superior to 30 % from ∼14 km. Regarding the vertical integration of the data, which reduce the statistical noise and extends the altitude range in the upper troposphere, it consists of an averaging window increasing with altitude. In the lower troposphere, since the backscattered signal is large, the initial resolution (150 m) is not degraded. In the middle and upper troposphere, the vertical resolution increases up to 2 km.

### 4.2 Calibration

One of the most important issues concerning the water vapour monitoring from Raman lidar technique is the calibration of the instrument (e.g., Sect. 2.1). Even if some procedures of independent calibration as well as calibration using $H_2O$ vertical total column have been explored (Sherlock et al., 1999b; Leblanc et al., 2008; Hoareau et al., 2009), the most common approaches consist of the normalization by radiosonde measurements. The lack of simultaneous and collocated radiosonde measurements over the site during the period 2002–2005 does not permit the use of them in this first investigation. Consequently, the calibration procedure has been performed using the ECMWF operational water vapour profiles. These data from the archive are re-sampled on a latitude-longitude resolution grid of 1.125°. Until August 2002, data used are provided on a vertical resolution of 21 pressure levels, after this date, the resolution is defined on 23 levels. To compare and calibrate lidar profiles with ECMWF profiles, relative humidity data provided by ECMWF were converted to water vapour mixing ratio by means of the empirical saturation vapour pressure over liquid water formulas of Hyland and Wexler (1983). The calibration coefficient is determinate by adjusting the water vapour lidar profile to the ECMWF one by the median of both profiles ratio at pressure levels of ECMWF data. Although this calibration method does not appear as the most appropriate method for the long-term commitment, it allows for a first assessment of the water vapour mixing ratio profiles dataset above La Reunion. The results indicate that the calibration coefficient values seem to be quite stable, with an observed mean variance of ∼13 %. When a major instrumental change occurs, the mean variance observed in the jump of the coefficient medians can be very important and change by a factor more than 10, as shown in Fig. 4.

## 5 Preliminary data investigations

### 5.1 Dataset

During 2002–2005 period, the water vapour Raman lidar system recorded about one hundred measurement nights. The $H_2O$ Raman channel being an additional channel of the existing Rayleigh-Mie lidar system, simultaneous measurements of water vapour and cirrus clouds have been realised. Based on the methodology regarding the integration time period described in Sect. 4.1, around 350 independent water vapour profiles have been obtained over this period with an average of 24 independent water vapour profiles per month. However, as seen in Fig. 5, there are more profiles from February to March and October to November. The reason for this is the duration of measurement acquisitions that were longer during these periods. This allows us to derive at more profiles in the same night given the high temporal and spatial variability of water vapour. On average, according to the water vapour variability, the integration time of the water vapour mixing ratio profiles is around 34 min (Fig. 6).

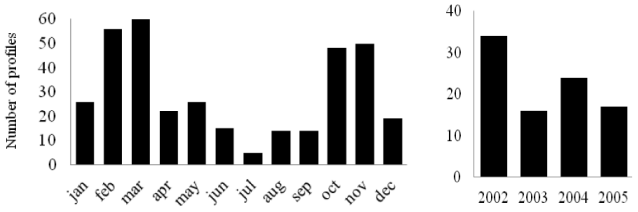



**Fig. 5.** Dataset histogram over the period 2002–2005.

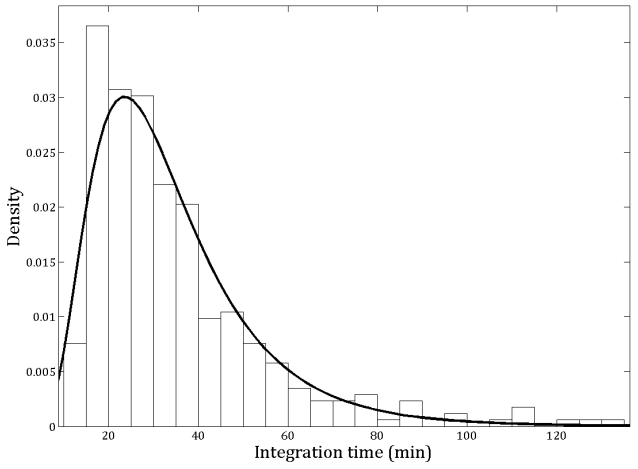



**Fig. 6.** Integration time distribution of the vertical profiles of water vapour mixing ratio. The bold black line represents a log-normal fit of the distribution which represents an adequate approximation of the histogram.

### 5.2 Water vapour seasonal cycle

The climatic context of the lidar station at La Reunion is typically that of an oceanic site dominated by the southern Hadley cell circulation (Baldy et al., 1996). Two typical seasons can be identified depending of the position of the Inter Tropical Convergence Zone (ITCZ) with respect to the island location. During the austral winter (May to October), the Inter Tropical Convergence Zone (ITCZ) position is distant from the island, and a strong influence of the Hadley and Walker cells generates steady easterly trade winds at low altitudes (<2 km) and westerly winds above the trade wind inversion (Taupin et al., 1999). During austral summer (November to April), the ITCZ comes within reach of the island and, thus, the trade wind influence is weaker. The trade wind inversion is almost entirely disappeared during the summer. Water vapour from the marine boundary layer can also be vented to the upper troposphere by intensive deep convection. Relating to these seasons and to these dynamical considerations, an analysis of the water vapour profiles is compared for the moist and dry seasons (Fig. 7). A mean ratio between both seasons about 1.6 up to 9 km is observed, above this altitude the ratio is in mean inferior to 0.4 until 15 km. From 9 km up to 15 km, the water vapour contents have a similar decrease for both seasons with mean values between $0.25\,g\,kg^{-1}$ at 9 km and $0.02\,g\,kg^{-1}$ at 15 km.

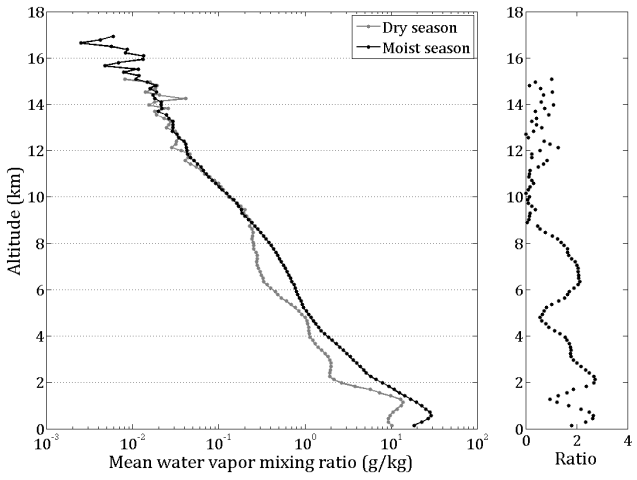



**Fig. 7.** Mean water vapour mixing ratio vertical profiles during the period 2002–2005 regarding the moist and dry season (left panel) and the ratio between the seasons (right panel).

### 5.3 Diurnal cycle

Based on water vapour distribution study at several altitudes, results have shown a systematic bimodal distribution in logscale of water vapour in the lower layer of the troposphere at all altitudes up to ∼4 km regarding mean distribution using all data available. However, this bi-modality in the distribution does not occur for each measurement. From one night to another, the distribution of water vapour mixing ratio can remain in one of the two modes or move from one mode toward another (Fig. 8). This variability seems to be in connection with the dynamical context of the island which is located in the influence of very regular east-south-easterly trade-wind. A wind inversion resulting from the descending branch of Hadley cell circulation is the main characteristic of the wind vertical distribution over Reunion: low-level easterlies are opposite to upper-level westerlies. The transition layer which delimits low-level trade-wind regime below and the upper westerly flow regime above, is known as the trade wind inversion (TWI) which is located between 2 and 5 km (Baray et al., 1998; Taupin et al., 1999). However, more investigations need to be performed for a better interpretation of these results. Steep topography, dynamical influence on the synoptic trade-wind flow and various diurnal thermal effects makes this a complex analysis.

### 5.4 Cirrus clouds analysis

In the upper troposphere, a fraction of the water condenses to generate cirrus clouds. Cirrus clouds are a main uncertainty in climate change assessments (Houghton et al., 2001). They have been identified as one important regulator of the

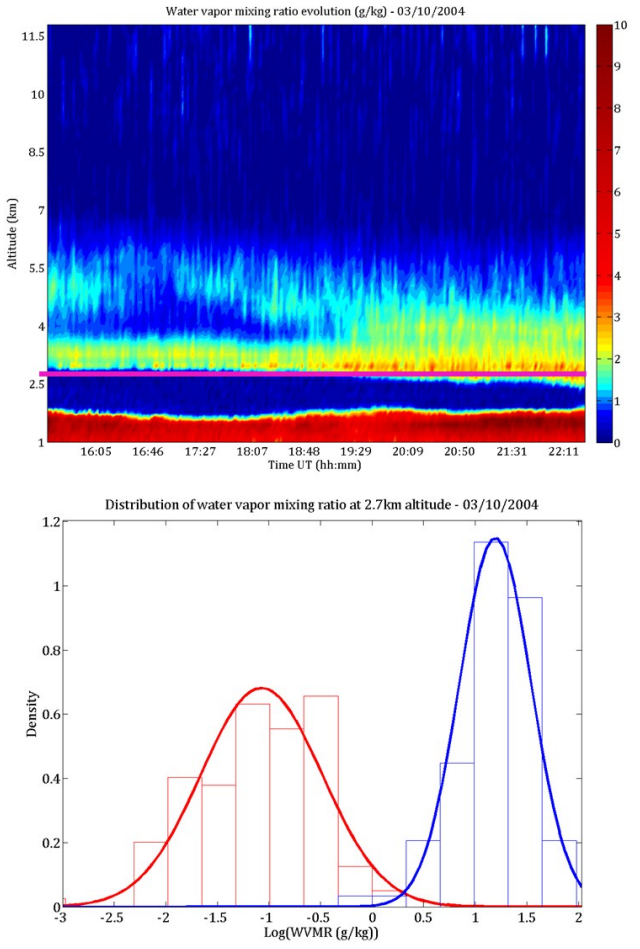



**Fig. 8.** Evolution of water vapour mixing ratio to 3 October 2004 (top panel). Pink dotted line represents an example of location (here at 2.7 km altitude) where the distribution of water vapour are bimodal (bottom panel). On the right panel, red line represents the water vapour distribution before 19:30 UTC and the blue line the distribution after 19:30 UTC.

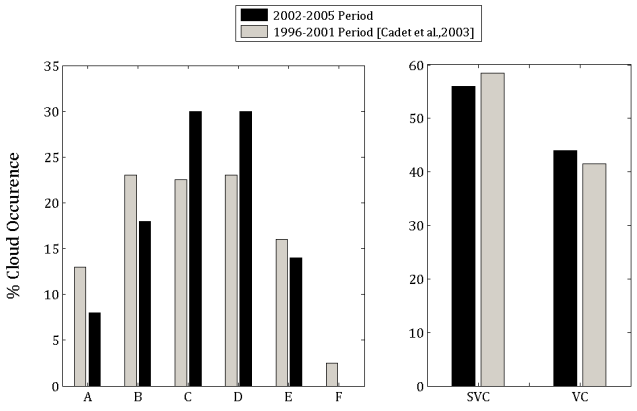



**Fig. 9.** Histograms of cirrus optical thickness binned on a log scale. Lettering along the abscissa (left panel) corresponds to the following optical thickness intervals: A = (0.001–0.003), B = (0.003–0.01), C = (0.01–0.03), D = (0.03–0.1), E = (0.1–0.3), F = (0.3–1.0). The right panel shows the combined results according to subvisible cirrus (SVC) and visible cirrus (VC). Categories A–C comprises the SVC component and D–F comprises the VC component.

radiation balance of the earth-atmosphere system (Twomey, 1991). It is important to investigate the altitude range and vertical extension of cirrus clouds, which are critical parameters for the radiative balance of the atmosphere. A cirrus cloud at high altitudes and, hence, a cold cloud, influences more strongly the infrared flux than the same cirrus at lower altitudes. In contrast, a cirrus cloud at low altitudes has a weaker effect (cirrus cloud reflecting back to space the incoming solar radiation). Currently, the vertical transport of water vapour and ice particles in the vicinity of the tropopause is not perfectly known. The processes involved are debated (Pommereau et al., 2011; Kiemle et al., 2008) and different formation processes could lead to different cloud characteristics that require identification before a specific statistical analysis (Keckhut et al., 2006). A first climatology of subtropical cirrus clouds from Reunion Island lidar dataset for the period 1996–2001 has been already published (Cadet et al., 2003). The updated analysis realised here for the period 2002–2005 is in good agreement with these previous results regarding the cirrus clouds optical depth distribution (Fig. 9). In both cases, the percentages have to be associated with the value of lidar ratio equal to 18.2 sr and subvisible cirrus (SVC) are defined with an optical depth $\tau \leq 0.03$ (Sassen et al., 1989). However, Cadet et al. (2003) indicated that the cirrus clouds occurred 7 % of the time for the total observation period versus 15 % for the updated analysis. Cirrus occurrence frequency is obtained as the ratio of cirrus detection time versus the total measurement time.

Moreover, complementary analyses have been performed regarding cirrus cloud classification according to geometrical macrophysic properties and some investigations regarding origin have been regarded. The optical thickness of cirrus cloud is calculated in accordance with the scattering ratio profile (SR) using a method as described in Sect. 2.2. In order to identify different cirrus cloud classes, a probability distribution study of diverse parameters of cirrus clouds (optical thickness, top, mean altitude and geometric depth of cirrus cloud) is realised. Results regarding the probability density functions (PDFs) show no single mode Gaussian distribution which suggests possible different types (Fig. 10). To discriminate the different classes, a cluster analysis is performed. The approach used is similar to the multivariate analysis performed by Keckhut et al. (2006) to discriminate different cirrus classes. It consists here of applying a Hierarchical Ascendant Classification (HAC) analysis on geometrical macrophysic cirrus clouds parameters (optical depth, top, mean altitude and geometric depth of cirrus clouds) derived from lidar measurements. Principle of the HAC consist to organise the observations, defined by a certain number of variables, in aggregating them hierarchically. This method assumes that

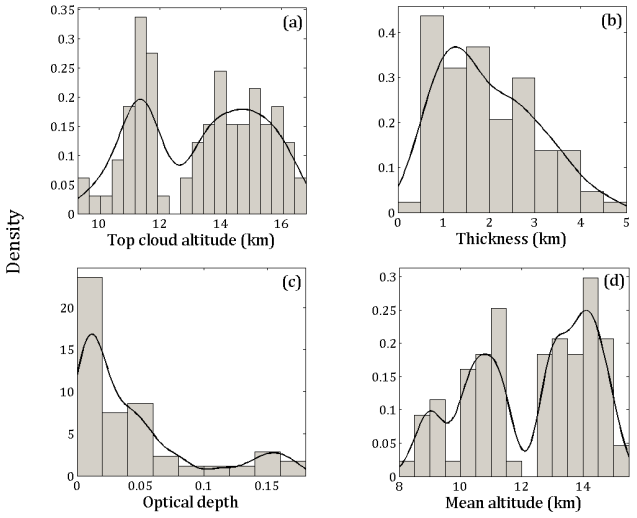



**Fig. 10.** Probability Density Function (PDF) of the different characteristics of cirrus clouds observed at Reunion Island over the period 2002–2005. The panels **(a)**, **(b)**, **(c)** and **(d)** represent, respectively, the top of cirrus clouds, geometrical thickness, the optical depth and the mean altitude.

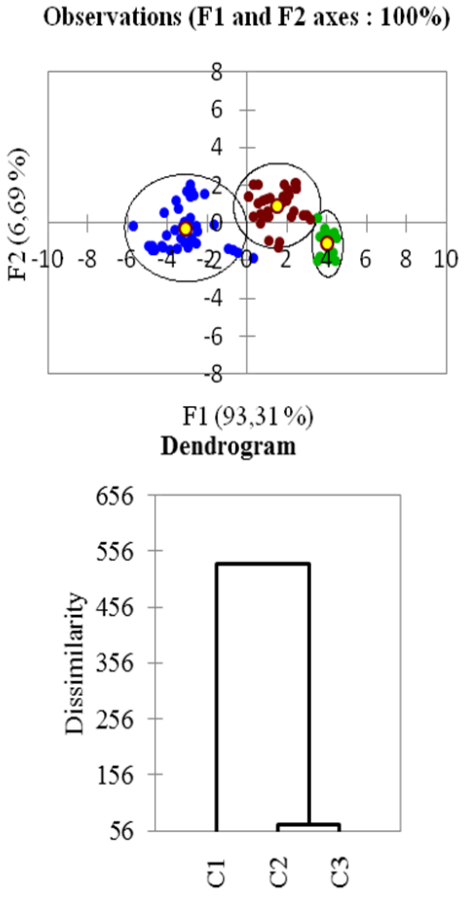



**Fig. 11.** Virtual representation of the observations on discriminated axis showing the different classes and performed from the discriminant factor analysis (on the top panel). Circles represent different identified classes with a confidence interval of 95 %. Blue dots represent the first class (midtroposphere thin cirrus), red dots represent the second one (thick upper troposphere cirrus) and the green dots represent the third class (upper troposphere thin cirrus). Dendogram derived from the hierarchical ascendant classification is shown on the bottom panel.

dissimilarity measure between the observations is existing and distance can be used as dissimilarity measure. In this study, dissimilarity is calculated using euclidean distance and the Ward's method, described in Ward (1963), is used for the agglomerative clustering method. Based on this analysis, HAC lead to three distinct classes as shown in Fig. 11. The mean and standard deviation for all parameters of each cirrus class are listed in Table 1. To ensure the robustness of these results, a discriminant factor analysis (DFA) is performed. DFA permits the identification of the optimal set of orthogonal projection axes which best separate the classes; these axes are the discriminant factor. As three classes have been previously identified, the analysis is done according two discriminants axes, F1 and F2. Results show a better discrimination of the different classes regarding the discriminant factor F1 which represents 93.31 % of discrimination (Fig. 11). Other results indicate 99 % of the correlation between the discriminant factor F1 and the top of cirrus clouds which seems to be the most important parameter for the discrimination of the classes. DFA corroborates to the HAC results at 98.85 % with only one different affection on 87 observations. A complementary analysis regarding the origin of the different classes is realised. Images from geostationary METEOSAT satellite are used in this analysis. During the 2002–2005 period, EUMETSAT (Europe's Meteorological Satellite Organisation) was operating the Meteosat 5 satellite providing centred observations over the Indian Ocean (repositioned at 63° E in 1998 for the Indian Ocean Experiment: INDOEX). Images used here are from infrared channel in spectral range 10.5–12.5 µm with resolution at nadir of 5 km and observations taken every 30 min. From the images, which have been linked with lidar observations, three types of atmospheric motions have been identified and appear to be associated with the different classes: middle latitude front, tropical convection and tropical cyclone. Among the different cirrus clouds classes obtained, the first one (Class I) is related to a middle latitude front with a top of cirrus cloud located at 11.3 km in mean and an occurrence of 44 %. The Class II and III are related to the tropical cyclone and tropical convection respectively (Fig. 12). For the Class II which is associated to the tropical cyclone, the top of cirrus clouds is located at 15.9 km and represents less of 20 % of occurrence. The mean geometrical thickness of the cirrus clouds belonging to this class is 3 km. The Class III indicates a mean altitude of 14.3 km for the top of cirrus clouds with thickness of cirrus around twice lower than the class II, 1.4 km, and an occurrence of 37 %.

**Table 1.** Characteristics of the three cirrus classes.

| Class type | I. Midtroposphere thin cirrus | II. Thick upper troposphere cirrus | III. Upper troposphere thin cirrus |
|---|---|---|---|
| Occurrence (%) | 44 | 19 | 37 |
| Mean altitude (km) | $10.3 \pm 0.9$ | $14.3 \pm 0.6$ | $13.6 \pm 0.6$ |
| Thickness (km) | $2 \pm 1.1$ | $3 \pm 0.7$ | $1.4 \pm 0.5$ |
| Optical depth | $0.04 \pm 0.04$ | $0.09 \pm 0.06$ | $0.02 \pm 0.02$ |
| Top altitude (km) | $11.3 \pm 0.8$ | $15.9 \pm 0.4$ | $14.3 \pm 0.6$ |

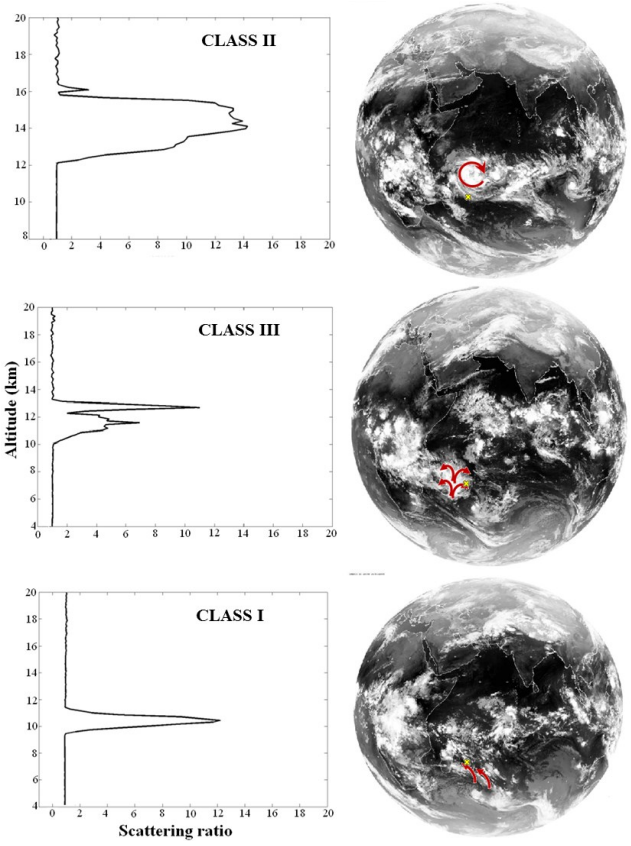



**Fig. 12.** Representation of different cirrus cloud classes. Left panels represent the scattering ratio profiles for each class and right panels represent the corresponding MeteoSat image. Reunion Island is indicated by a yellow cross. Atmospheric move is represented by red arrows. The corresponding dates are 16 March 2005, 15 December 2004 and 9 February 2003 (from the top to the bottom).

## 6 Future lidar system

The results presented in Sect. 5 demonstrate the capabilities of water vapour monitoring in upper troposphere from lidar instrument over a subtropical site. The challenge is now to monitor water vapour with a lidar system able to measure in the upper troposphere with a smaller random error and to reach the lower stratosphere. The future Raman lidar which will be implemented in Piton Maïdo facility at Reunion Island at the end of 2011 is designed to reach UTLS. The station is located above the boundary layer, in the less cloudy part of the island at an altitude of 2200 m a.s.l. The future instrument, under construction, is principally dedicated for the water vapour measurements in the lower stratosphere and upper troposphere, but also for the measurements of stratospheric temperature using Rayleigh scattering. It will detect light backscattered by molecules and particles in the atmosphere from outgoing laser beam at 355 nm. Inelastic Raman backscatter from nitrogen will be detected at 387 nm. It will allow the direct retrieval of the aerosol extinction coefficient $\alpha$ and will be used to retrieve the water vapour mixing ratio using the channels at 407 nm which will detect vibrational Raman scattering from $H_2O$ molecules.

### 6.1 Choice of the excitation wavelength

The emitted wavelength was chosen to improve the overall efficiency and is based on several factors: water vapour backscattering cross-section, laser source availability and power, detector efficiency. Molecular scattering follows a $\lambda^{-4}$ law, therefore, short wavelengths are more efficient and the near ultraviolet (UV) band is the most indicated. UV bands allow better detector efficiency than in the visible and near infrared bands. The light source of this lidar consists in two commercial Quanta Ray Pro-290-30 Nd:Yag lasers with frequency tripling, generating laser pulses with about 375 mJ at 355 nm with a repetition rate of 30 Hz and a duration pulse of 9 ns. Pulses of both lasers can be synchronized and output beams can be coupled through polarization cubes to emit 750 mJ pulses at 355 nm. This flexibility will enable a power increase, if needed, to reach UTLS. The lidar design was built with the opportunity to use both emitting wavelength. While capabilities are expected to be similar in theory, the design will allow direct comparisons including calibration and operational issues. In the laser coupling and optics design, we also thought about using both lasers emitting at 532 nm for potential intercomparison and, for operational reasons, it was decided to change.

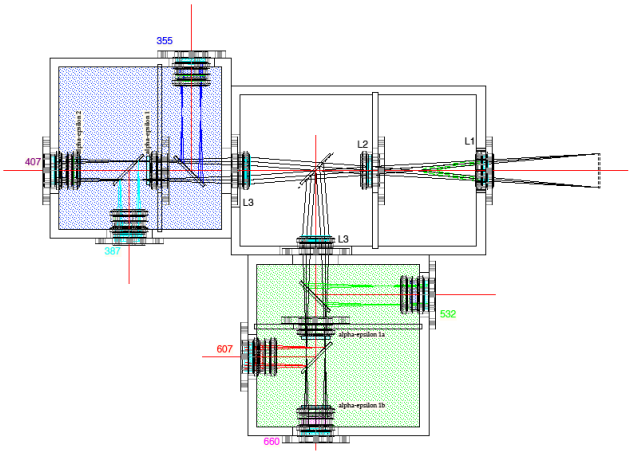



**Fig. 13.** Schematic view of the optical ensemble of the future lidar implemented at Observatoire de Physique de l'Atmosphère de La Réunion (OPAR).

### 6.2 Optical ensemble

Regarding the optical ensemble, the radiation backscattered by the atmosphere is collected by a 1.2 m – diameter telescope that was previously used at Biscarrosse for Rayleigh temperature and Raman measurements (Hauchecorne et al., 1991; Keckhut et al., 1990). A narrow field-of-view of 0.25 mrad will be used to reduce, as little as possible, sky background and detector noise. Contrary to the lidar system used during the period 2002–2005, the future one will not use optical fibres in the focal plane of the telescope to transfer the backscattered signals to the optical ensemble. This will avoid a systematic bias in water vapour measurements due to fluorescence contribution in fibre-optic cables, even if this transfer protocol permits us to obtain quasi-constant illumination conditions at the optical fibre output and that even telescope alignment changes. This is not the case in conventional systems (without optical fibre) where optical alignment change can lead to important variations (∼2–5 %) in the response system due to detector spatial inhomogeneities and, thus, the calibration coefficient (Whiteman et al., 1992; Nedeljkovic et al., 1993). However, even if OH-rich fibres were used for the preliminary system, resulting in a reduction in the estimated fluorescence contribution, the bias introduced by the fibre fluorescence can be significant to be corrected for on a routine basis (Sherlock et al., 1999a). Consequently, we designed a configuration with a direct optical path between the secondary mirror of the receiver and the detection box, although fluorescence is not limited to the fibre-optics and could arise in any optical component. Careful tests will be required when lidar is implemented.

### 6.3 Rayleigh-Mie and Raman signals separation

The backscattered signals collected by the telescope are, firstly, transferred toward an optical ensemble through a set of lenses and mirrors. A spectral separation of the light is then realised through a set of dichroic beam splitters as well as BPIF. A schematic view of the optical ensemble is shown in Fig. 13. The beam reflected is split by dichroic beam splitter that reflects 532 nm component toward an auxiliary optical ensemble. The filtered beam is then split by another dichroic beam splitter that reflects its 355 nm component toward the photomultiplier of the Rayleigh-Mie channel coupled with a BPIF with a maximum transmission of 55.3 %. The transmitted beam is filtered by a high-pass interference filter designed to reject the remaining at 355 nm. This filter has a maximum transmission of 90 % and 85 % at 407 nm and 387 nm, respectively. Another dichroic beam splitter is then used to reflect the 387 nm component toward the photomultiplier of the $N_2$ Raman channel and transmits its 407 nm component toward the photomultiplier of the $H_2O$ Raman channel. A BPIF with a maximum transmission of 63.7 % at 387 nm and a FWHM of 3 nm is placed in the front of the $N_2$ PMT. A high-pass interference filter designed to reject the remaining 387 nm component and a BPIF are placed between the last dichroic beam filter and the lens which focalized the beam onto the photocathode of the $H_2O$ PMT. The BPIF has a maximum transmission of 60.6 % at 407 nm and a FWHM of 1 nm. In case we decided to work in visible wavelengths in the future, the optical subsystem containing the splitters, dichroic mirrors and detectors can be upgraded with a second ensemble adapted to the useful wavelengths.

### 6.4 Photo detection

In theory, the limiting factor for a PMT in photon counting mode is the dark current. This current that contributes to the noise in the measurements can be used to categorise the limit of detection of a PMT. It can be expressed in term of Equivalent Noise Input (ENI) that is an indication of the photon-limited signal-to-noise ratio. It refers to the amount of light to produce a signal-to-noise of unity in the output of PMT and can be expressed as follows:

$$\mathrm{ENI} = \frac{\sqrt{2q\,\mathrm{ldb}\,G\,\Delta f}}{S} \tag{3}$$

where $q$ is the electronic charge, ldb is the anode dark current (A), $G$ is the gain, $\Delta f$ is the bandwidth of the system (Hz) and $S$ is the anode radiant sensitivity at the wavelength of peak response ($\mathrm{A\,W^{-1}}$).

Relating to the photon detector, we will use new Hamamatsu R7400-03 g or 20 g mini-photomultiplier tubes depending of the wavelengths we will emit; R7400-03 g for an emitted wavelength at 355 nm and the R7400-20 g at 532 nm. Although an emitted wavelength at 355 nm is mostly indicated and will be principally used, we will dispose of an

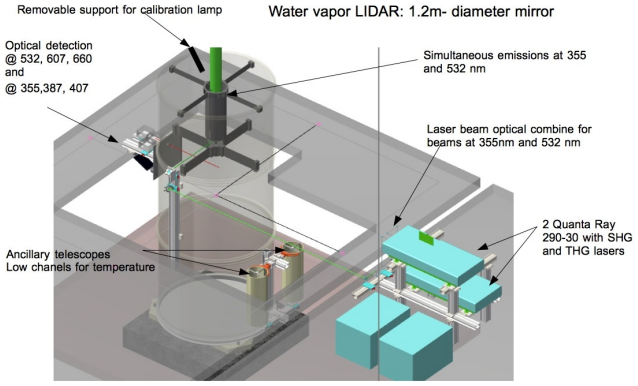



**Fig. 14.** Representation of the design of the future lidar implemented at the Reunion Island altitude observatory.

auxiliary optical ensemble which can be used simultaneously for received wavelength at 607 nm and 660 nm, since a simultaneous emission at 532 nm and 355 nm can be performed (Sect. 6.1). The R7400-03 g has a typical spectral response in UV-Visible with a cathode radiant sensitivity of $\sim$60 m A W$^{-1}$ for the wavelength 387 nm and 407 nm. Regarding the R7400-20 g, the spectral response is located in the Visible-Near IR range with a cathode radiant sensitivity of $\sim$75 m A W$^{-1}$ for the wavelength 607 nm and 660 nm. Although these tubes are less sensitive than old cooled R1477, smaller ENI have been indicated for Hamamatsu R7400-03 compared to Hamamatsu R1477 at wavelengths 355 nm, 387 nm and 407 nm, with a decrease of $\sim$40 %, $\sim$30 % and $\sim$20 %, respectively, of the ENI values. However, we will need to check which PMT to give a better performance with different emitted energy per pulse. Regarding data acquisition for Raman channels, we will use TR 20–160 transient recorders for both analog (lower altitude) and photon-counting (upper altitude) combination increasing the dynamical range of acquired signal compared to conventional system. This requires post processing analysis, which involves the merging of the analog and photon counting signals into a single return signal through either a process known as "gluing", in which the photon counting and analog signals are initially corrected for photon pulse pile-up correction and delay, respectively, (Whiteman et al., 2006; Newsom et al., 2009) or more recently in using the maximum-likelihood method (Veberic, 2012). By combining the signals through these procedures, we take advantage of the superior sensitivity of the photon counting data in the weak signal regime and the improved linearity of the analog data in the strong signal regime.

### 6.5 Calibration

Regarding the future calibration of the instrument, coaxial geometry for emission and reception was chosen, as shown in Fig. 14; indeed this design will avoid parallax effect, extend measurement down to the ground and contribute to ease the alignment. It will allow us to perform, in better conditions, calibration using $H_2O$ total column measurements from collocated ancillary instruments (GPS, radiometer,...). Radiosonde data, which could be realised on a daily basis at the meteorological station (20 km faraway), could be used for comparison on the full height range. These measurements will be used as a fully independent and systematic duplicate measurement for the comparison with water vapour lidar profile calibrated from $H_2O$ total column measurements. Indeed, the distance between lidar and radiosonde sites could not be very effective for that which concerns calibration. However, to compare one calibration method to another, some methodology to calibrate through noncollocated radiosoundings (with similar range of noncollocation) can be used if need be (Dionisi et al., 2010). In the mechanical design, we defined and built an integrated and removable support for a calibration lamp to complement the calibration with total $H_2O$ measurements to use the hybrid technique. Although instrumental changes can be detected following calibration method using radiosondes, those using calibration from lamp or passive zenith daytime observations are better. It is, therefore, important to implement one of these methods for the instrument monitoring, which is necessary for long term monitoring.

### 6.6 Numerical evaluation of lidar signals

Numerical simulations of lidar signals can be performed for studying the expected system capability. The range interval for which a lidar can be operational is limited by the geometrical form factor function and saturation in the lower altitude and the fast decreasing signal-to-noise ratio (SNR) at far altitude range. For a first performance simulation, we suppose the R7400-03 Hamamatsu PMT with a typical dark count rate of 80 s$^{-1}$ to evaluate the detector-noise contribution compared to sky background in measurements. The quantum efficiency of the R7400-03 PMT is around 22 % for 407 nm wavelength. Based on these component properties and $H_2O$ channel efficiency (Table 2), simple numerical simulation of the system performance has been performed and compared to the previous system which used SPCM AQ-232 APD for $H_2O$ channel.

For measurements at a given emitted wavelength $\lambda_0$, the lidar signal $N(\lambda_H, z)$ in photon counts, corresponding to the range $z$, can be calculated by the following equation:

$$N(\lambda_H, x) = \frac{K}{z^2} n_H(z) \frac{d\sigma_H(\pi)}{d\Omega} e^{(-[\int_0^z \alpha(\lambda_0, z')dz' + \int_0^z \alpha(\lambda_H, z')dz'])} + N_0 + N_D \quad (4)$$

where $K$ is a proportionality constant for $H_2O$ channel that accounts for the system optical efficiency, the telescope receiver area, the photomultiplier tube (PMT) spectral efficiency, the overlap function and the laser output energy; $d\sigma_H(\pi)/d\Omega$ is the Raman backscattering cross-section

**Table 2.** System Parameters for $H_2O$ channel for the actual and future lidar system.

| System parameter | Parameter value | |
|---|---|---|
| | Actual lidar | Future lidar |
| Received wavelengths | 660.5 nm | 407.5 nm |
| Filter bandwidth | 1 nm | 1 nm |
| Filter transmission | 0.14 | 0.39 |
| Detector | EG&G SPCM AQ −232 photodiode | R7400-03 Hama matsu photomultiplier |
| Quantum efficiency | 0.35 | 0.22 |
| Total $H_2O$ channel efficiency | 3.2 % | 7.6 % |

**Table 3.** Sky Spectral Radiance for different weather conditions and corresponding sky background for the $H_2O$ channel future lidar system (integration time of 30 min is considered).

| Reference | λ [nm] | Period | $L_\lambda$ [W m$^{-2}$ sr$^{-1}$ nm$^{-1}$] | $N_0$ | $N_0/N_D$ |
|---|---|---|---|---|---|
| Höhn and Büchtemann (1973) | 400 | Night (1,2) | $3.4.10^{-9}$ | 0.34 | 0.08 |
| Höhn and Büchtemann (1973) | 400 | Night (3) | $1.9.10^{-8}$ | 1.95 | 0.45 |
| Höhn and Büchtemann (1973) | 400 | Night (4) | $5.10^{-8}$ | 5.14 | 1.19 |

(1) Clear sky (moonless), (2) thinly covered sky, haze or thin fog (moonless), (3) clear sky (moonlit), (4) thinly covered sky, haze or thin fog (moonlit). The typical dark count rate of R7400-03 Hamamatsu photomultiplier $d = 80\,s^{-1}$ is used. $N_0$ and $N_D$ are, respectively, the night sky background and the detector noise (in photon).

for $H_2O$ molecule; $n_H(z)$ is the $H_2O$ number density; the exponential factor gives the two-way atmospheric transmission, where $\alpha$ is the total extinction coefficient; $N_0$ is the sky background and $N_D$ represents the detector dark counts.

The background term can be evaluated as follows:

$$N_0 = n_0 n_q \frac{\lambda_H}{hc} W A f \Delta t \Delta\lambda_H \frac{2\Delta R}{c} \Omega \quad (5)$$

where $W$ is the background radiance (W sr$^{-1}$ nm$^{-1}$ m$^{-2}$), $\Delta\lambda_H$ is the receiver bandwidth (nm), and $\Omega$ is the observation solid angle (sr), $\eta_0$ the efficiency of the received channel, $\eta_q$ the quantum efficiency, $\Delta t$ the integration time (s), $\Delta R$ the vertical resolution (m), $h$ the Planck constant and $c$ the speed of light. And the dark count rate, expressed in function of $d$ (s$^{-1}$), can be estimated as follows:

$$N_D = \frac{2f}{c} d \Delta R \Delta t \quad (6)$$

To perform the numerical simulations, water vapour mixing ratio profiles from ECMWF ERA-40 re-analysis is used as reference profile, and the atmospheric profile has been derived by taking into account extinction due to Rayleigh scattering. Rayleigh scattering profiles have been computed using International Standard Atmosphere. Absorption by ozone and other trace gases is negligible at the wavelengths used and the extinction due to aerosol have not been considered due to altitude station (2200 m). Due to the large bandwidth of the interferential filter (1 nm), no temperature dependence corrections have performed. Based on measurements on the 15 March 2005 for the current system, the detector noise ($N_D$) to sky background ($N_0$) ratio has been shown to be around 2. Indeed, based on the lidar measurements for this date, which have been performed in clear sky and moonless conditions, the background noise indicated a value of ∼20.5 photons for a 30 min time integration as shown in Fig. 15. From this observation and based on APD dark count tests conducted in the same weather conditions, with values found close to 250 s$^{-1}$ for the APD dark counts, the derived value is ∼13.5 and 6.9 photons for the detector dark counts and sky background, respectively, according to the Eqs. (5) and (6). The derived night sky radiance of $4.6.10^{-9}$ W m$^2$ sr$^{-1}$ nm$^{-1}$ is in agreement with the night sky radiance range values indicated in literature at return wavelength and similar weather conditions (Höhn and Büchtemann, 1973; Turnrose, 1974). Höhn and Büchtemann (1973) measured the sky brightness from 400 to 800 nm in a range of weather conditions and under various aspects both experimentally and theoretically. We chose their spectrum to estimate night sky radiance and perform the numerical simulations for the future lidar system (Table 3). Usually to reduce the statistical noise, in addition to the temporal integration and to extend the altitude range in the upper troposphere, vertical integration is applied. In the numerical simulations, only temporal integration has been regarded according to mean time integration (∼30 min) which corresponds to the mean time integration to access water vapour variability, as described in Sect. 5.1.

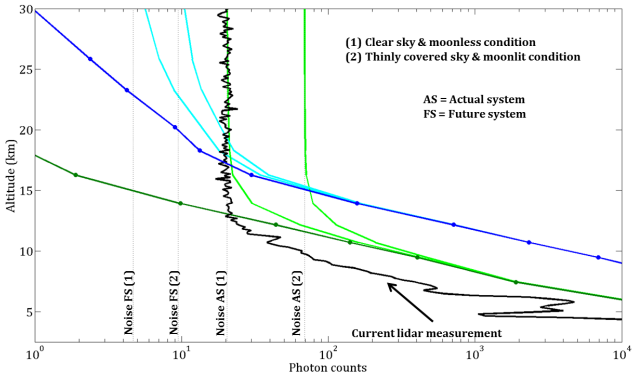



**Fig. 15.** Raman $H_2O$ backscattered signal comparison (30 minutes time integration). The bold black line with dots corresponds to the numerical simulation regarding the current lidar system and the bold black line with a square for the future one with one laser. The grey lines correspond to the numerical simulation + noise (sky background and detector noise) following different weather conditions: dark grey lines for the actual system and light grey lines for the future system. Weather conditions are indicated on the figure.

Concerning the water vapour signal strength, simulations indicate a ratio of ∼150 at lower altitude (∼3 km) with a decrease to ∼20 around the tropopause (∼16 km) between both lidar systems for Raman $H_2O$ channel for one laser in operation at 355 nm (Fig. 15). This ratio decrease is essentially due to the altitude squared dependence in return signal which is not the same due to the altitude difference between both stations (∼2100 m). Although performances improvement are the result of the emission wavelength which implies a greater backscattering of molecules at return wavelength, the receiver area and detection efficiency, the altitude of the station permits the improving of the backscattered power principally in lower altitude since the factor is ∼11 at ∼3 km and decreases to ∼1.3 at ∼16 km. In this development stage, the altitude expected within an error of 15 % for $H_2O$ measurements, regarding random error (principally sky background and photon counting error) and a pre-accumulated signal of 30 min is of ∼15.6 km in clear sky and moonless condition and ∼15.5 km with thinly covered sky and moonlit. For the same measuring conditions, random error reaches 30 %, respectively, at around ∼18 km and ∼17.6 km. Coupling both lasers, the altitude expected within an error of 15 % and 30 % are 16.8 km and 21 km, respectively, for clear sky and moonless condition.

Concerning the actual system, simulation results have been compared to the experimental measurements. Comparison indicated a ratio of ∼4 for $H_2O$ channel between the expected results from simulation and those from the instrument. And regarding the numerical simulation, the expected altitude for a random error at 15 % and 30 % is, respectively, around 11.8 km and 13 km in clear sky and moonless conditions. In comparison, assuming that the same factor of 4 between both experimental and simulation results and that seems to better correspond with real-world expectations, we could expect to reach an altitude of 14.6 km and 16.3 km within 15 % and 30 %, respectively, and good weather conditions.

## 7 Conclusions

We have presented preliminary data of water in upper troposphere from lidar instrument over a subtropical site. Performing analysis of the preliminary system lidar dataset, advantages and drawbacks have been pointed out. The present configuration of the lidar system permits the covering of a large altitude range, from the ground up to the upper troposphere (∼14–15 km) within a random error of 30 % for a temporal integration of ∼50 min, vertical integration up to ∼2 km, during nighttime and presence of any clouds. Regarding statistical analysis, some results based around 350 independent water vapour profiles have been presented. Mean vertical profiles of water vapour in respect of the seasons have shown a mean ratio of 1.6 up to 9 km. This ratio decreases within 0.4 in mean between both seasons above 9 km up to 15 km. About cirrus cloud analysis, according to different parameters of cirrus clouds, 3 distinct classes have been obtained. Following these different classes and complementary analysis based on Meteosat images, origin of the classes have been identified and related to the tropical convection (class III), tropical cyclone (class II) and midlatitude front (class I); with 37, 19 and 44 %, respectively, of occurrence. The most discriminatory parameter associated with the classification seems to be the top of the cirrus cloud. These altitudes have been demonstrated at 11.3 km for the first class I, 15.9 km for the second, and 14.3 km for the third. Although these analyses have shown good results regarding water vapour and cirrus data, some aspects needed to be resolved in order to improve the measurements from the future lidar system. Based on these analyses and encountered difficulties to derive water vapour mixing ratio profiles, the characteristics and the future design of the instrument deployed to the Maïdo station has been presented. According to a simple numerical simulation of the system performance, the results have shown a ratio of 4 for $H_2O$ channel between theoretical curves and instrumental measurements with one laser in operation. The maximum altitude expected, taking into account a random error within 15 % and pre-accumulated signal of 30 min, has been indicated at 11.8 km for $H_2O$ channel in clear sky and moonless condition. Based on characteristics and design of the future lidar system, and regarding the numerical simulation of both systems, the performances seem to be improved by a factor 20 for $H_2O$ channel around 16 km. The improvements of these performances are principally due to a better detection efficiency of the optical ensemble and backscattering cross-section at shorter wavelength, the size of the telescope and the altitude of the new observatory (2200 m a.s.l.) which permit to improve the backscatter

power of a ratio ∼150 at ∼3 km. Concerning the design of the future instrument, some modifications have been chosen compared to the preliminary system in order to avoid systematic bias in water measurements removing the optical fibre and to facilitate the calibration choosing coaxial emission. Consequently, with an expected altitude between 14.6 km and 16.8 km for $H_2O$ channel, within a random error of 15 % and a temporal integration of 30 min, and regarding the characteristics and the design of the future lidar system and different calibration aspects, this lidar could be suitable for long-term monitoring of water in the upper troposphere – lower stratosphere. The future system will allow us to provide data for the validation of present satellite experiences like AURA-MLS, AQUA-AIRS and more recently the Indian-French project MEGHA TROPIQUES which was launched at the end of 2011 and which hosted the instrument SAPHIR (micro-wave radiometer). Flexibility in the design (emitted power, wavelengths, calibration techniques,. . . ) will enable to improve the performances of this instrument in the long-term to fully reach on operational system in the tropic for water vapour monitoring up to the low stratosphere.

*Acknowledgements.* Reunion Island Atmospheric measurements are supported by French regional, national (INSU/CNRS), and European funding. We are grateful to Jean-Marc Metzger, Françoise Posny and Nadège Montoux for their help in performing the CFH measurements and to Jean Leveau, Serge Baldy and Robert Delmas for their contribution to instrumental development at Reunion Island. We acknowledge the European Centre for Medium range Weather Forecasts (Reading, England) for providing global model data and the NERC Satellite Receiving Station (Dundee University, Scotland) for providing the Meteosat data.

Edited by: A. Lambert




The publication of this article is financed by CNRS-INSU.

## References

Acharya, Y. B., Sharma, S., and Chandra, H.: Signal induced noise in PMT detection of lidar signals, Measurement, 35, 269–276, 2004.

Baldy, S., Ancellet, G., Bessafi, M., Badr, A., and Lan Sun Luk, D.: Field observations of the vertical distribution of tropospheric ozone at the island of Reunion (southern tropics), J. Geophys. Res., 101, 23835–23849, 1996.

Barray, J.-L., Ancellet, G., Taupin, F. G., Bessafi, M., Baldy, S., and Keckhut, P.: Subtropical tropopause break as a possible stratospheric source of ozone in the tropical troposphere, J. Atmos. Sol.-Terr. Phys., 60, 27–36, 1998.

Baray, J.-L., Leveau, J., Baldi, S., Jouzel, J., Keckhut, P., Bergametti, G., Ancellet, G., Bencherif, H., Cadet, B., Carleer, M., David, C., De Mazière, M., Faduilhe, D., Godin Beekmann, S., Goloub, P., Goutail, F., Metzger, J. M., Morel, B., Pommereau, J. P., Porteneuve, J., Portafaix, T., Posny, F., Robert, L., and Van Roozendael, M.: An instrumented station for the survey of ozone and climate change in the southern tropics: Scientific motivation, technical description and future plans, J. Environ. Monit., 8, 1020–1028, 2006.

Cadet, B., Goldfarb, L., Faduilhe, D., Baldy, S., Giraud, V., Keckhut, P., and Rechou, A.: A sub-tropical cirrus clouds climatology from Reunion Island (21° S, 55° E) lidar data set, Geophys. Res. Lett., 30, 30.1–30.4, 2003.

Cadet, B., Giraud, V., Haeffelin, M., Keckhut, P., Rechou, A., and Baldy, S.: Improved retrievals of the optical properties of cirrus clouds by a combination of lidar methods, Appl. Opt., 44, 1726–1734, 2005.

Cooney, J.: Remote measurement of atmospheric water vapour profiles using Raman component of laser backscatter, J. Appl. Meteorol., 9, 182–184, 1970.

Dionisi, D., Congeduti, F., Liberti, G. L., and Cardillo, F.: Calibration of a Multichannel Water Vapor Raman Lidar through Noncollocated Operational Soundings: Optimization and Characterization of Accuracy and Variability, J. Atmos. Ocean. Technol., 27, 108–121, 2010.

Faduilhe, D., Keckhut, P., Bencherif, H., Robert, L., and Baldy, S.: Stratospheric temperature monitoring using a vibrational Raman lidar. Part 1: Aerosols and ozone interferences, J. Environ. Monit., 7, 357–364, 2005.

Ferrare, R. A., Melfi, S. H., Whiteman, D. N., Evans, K. D., Schmidlin, F. J., and Starr, D. O'C.: A comparison of water vapour measurements made by Raman lidar and radiosondes, J. Atmos. Ocean. Technol., 12, 1177–1195, 1995.

Ferrare, R. A., Turner, D. D., Heilman Brasseur, L., Feltz, W. F., Dubovick, O., and Tooman, T. P.: Raman lidar measurements of the aerosol extinction-to-backscatter ratio over the Southern Great Plains, J. Geophys. Res., 106, 20333–20347, 2001.

Forster, P. M. de F. and Shine, K. P.: Assessing the climate impact of trends in stratospheric water vapour, Geophys. Res. Lett., 29, 1086, doi:10.1029/2001GL013909, 2002.

Goldfarb, L., Keckhut, P., Chanin, M.-L., and Hauchecorne, A.: Cirrus climatological results from lidar measurements at OHP (44° N, 6° E), Geophys. Res. Lett., 28, 1687–1690, 2001.

Hauchecorne, A., Chanin, M.-L., and Keckhut, P.: Climatology and trends of the middle atmospheric temperature (33–87 km) as seen by Rayleigh LIDAR over the South of France, J. Geophys. Res., 96, 15297–15309, 1991.

Hoareau, C., Keckhut, P., Baray, J.-L., Sarkissian, A., and Durry, G.: Methodology for water monitoring in the upper troposphere with Raman lidar at Observatory of Haute-Provence, J. Atmos. Ocean. Technol., 26, 2149–2160, 2009.

Höhn, D. H. and Büchtemann, W.: Spectral radiance in the S20-range and luminance of the clear and overcast night sky, Appl. Opt., 12, 52–61, 1973.

Houghton, J. T., Ding, Y., Griggs, D. J., Noguer, M., Van Der Linden, P. J., Dai, X., Maskell, K., and Johnson, C. A. (Eds.): Climate Change 2001: The Scientist Basis, Cambridge University

Press, 892 pp., 2001.

Hyland, R. W. and Wexler, A.: Formulations for the thermodynamic properties of the saturated phases of $H_2O$ from 173.15K to 473.15K, ASHRAE Tran., 89, 500–519, 1983.

Keckhut, P., Chanin, M.-L., and Hauchecorne, A.: Stratosphere temperature measurement using Raman Lidar, Appl. Opt., 29, 5182–5186, 1990.

Keckhut, P., Borchi, F., Bekki, S., Hauchecorne, A., and Silaouina, M.: Cirrus classification at midlatitude from systematic lidar observations, J. Appl. Meteor. Clim., 45, 249–258, 2006.

Kiemle, C., Wirth, M., Fix, A., Ehret, G., Schumann, U., Gardiner, T., Schiller, C., Sitnikov, N., and Stiller, G.: First airborne water vapour lidar measurements in the tropical upper troposphere and mid-latitudes lower stratosphere: accuracy evaluation and intercomparisons with other instruments, Atmos. Chem. Phys., 8, 5245–5261, doi:10.5194/acp-8-5245-2008, 2008.

Kirk-Davidoff, D. B., Anderson, J. G., Hintsa, E. J., and Keith, D. W.: The effect of climate change on ozone depletion through stratospheric water vapour, Nature, 402, 399–402, 1999.

Kley, D., Russell III, J. M., and Philips, C. (Eds.): SPARC assessement of upper tropospheric and stratospheric water vapour. WCRP 113, WMO/TD 1043, SPARC Rep. 2, 312 pp., 2000.

Leblanc, T. and McDermid, I. S.: Accuracy of Raman lidar water vapour calibration and its applicability to long-term measurements, Appl. Opt., 47, 5592–5602, 2008.

Leblanc, T. and McDermid, I. S.: Reply to "Comments on Accuracy of Raman lidar water vapour calibration and its applicability to long-term measurements" by Whiteman et al., Appl. Opt., 50, 2177–2178, 2011.

Leblanc, T., McDermid, I. S., and Raspey, R. A.: First-year operation of a new water vapour Raman lidar at the JPL Table Mountain Facility, California, J. Atmos. Ocean. Technol., 25, 1454–1462, 2008.

Nedeljkovic, D., Hauchecorne, A., and Chanin, M.-L.: Rotational Raman lidar to measure the atmospheric temperature from the ground to 30km, IEEE T. Geosci. Remote Se., 31, 90–101, 1993.

Newsom, R. K., Turner, D. D., Mielke, B., Clayton, M., Ferrare, R., and Sivaraman, C.: Simultaneous analog and photon counting detection for Raman lidar, App. Opt., 48, 3903–3914, 2009.

Platt, C. M. R. and Dilley, A. C.: Determination of the cirrus particle single-scattering phase function from lidar and solar radiometric data, Appl. Opt., 23, 380–386, 1984.

Pommereau, J.-P., Garnier, A., Held, G., Gomes, A. M., Goutail, F., Durry, G., Borchi, F., Hauchecorne, A., Montoux, N., Cocquerez, P., Letrenne, G., Vial, F., Hertzog, A., Legras, B., Pisso, I., Pyle, J. A., Harris, N. R. P., Jones, R. L., Robinson, A. D., Hansford, G., Eden, L., Gardiner, T., Swann, N., Knudsen, B., Larsen, N., Nielsen, J. K., Christensen, T., Cairo, F., Fierli, F., Pirre, M., Marécal, V., Huret, N., Rivière, E. D., Coe, H., Grosvenor, D., Edvarsen, K., Di Donfrancesco, G., Ricaud, P., Berthelier, J.-J., Godefroy, M., Seran, E., Longo, K., and Freitas, S.: An overview of the HIBISCUS campaign, Atmos. Chem. Phys., 11, 2309–2339, doi:10.5194/acp-11-2309-2011, 2011.

Reichardt, J., Reichardt, S., Behrendt, A., and McGee, T. J.: Correlations among the optical properties of cirrus-clouds particles: Implications for spaceborne remote sensing, Geophys. Res. Lett., 29, 1668, doi:10.1029/2002GL014836, 2002.

Sakai, T., Nagai, T., and Nakazato, M.: Comparisons of Raman lidar measurements of tropospheric water vapour profiles with radiosondes, Hygrometers on the Meteorological Observation Tower, and GPS at Tsukuba, Japon, J. Atmos. Ocean. Technol., 24, 1407–1423, 2007.

Sassen, K., Griffin, M., and Dodd, G.: Optical scattering and microphysical properties of subvisual cirrus clouds, and climatic implications, J. Appl. Meteorol., 28, 91–98, 1989.

Seidel, D. J., Fu, Q., Randel, W. J., and Reichler, T. J.: Widening of the tropical belt in a changing climate, Nature, 1, 21–24, 2008.

Sherlock, V. J., Garnier, A., Hauchecorne, A., and Keckhut, P.: Implementation and validation of a Raman lidar measurement of middle and upper tropospheric water vapour, Appl. Opt., 38, 5838–5850, 1999a.

Sherlock, V. J., Hauchecorne, A., and Lenoble, J.: Methodology for the independent calibration of Raman backscatter water vapour lidar systems, Appl. Opt., 38, 5816–5837, 1999b.

Soden, B. J. and Lanzante, J. R.: An assessment of satellite and radiosonde climatologies of upper-tropospheric water vapour, J. Climate, 9, 1235–1250, 1996.

Taupin, F. G., Bessafi, M., Baldy, S., and Bremaud, P. J.: Tropospheric ozone above the southwestern Indian Ocean is strongly linked to dynamical conditions prevailing in the tropics, J. Geophys. Res., 104, 8057–8066, 1999.

Turnrose, B. E.: Absolute energy distribution of the night sky at Palomar and Mount Wilson Observatories, Publ. Astron. Soc. Pac., 86, 545–551, 1974.

Twomey, S.: Aerosols, clouds and radiation, Atmos. Environ., 25, 2435–2442, 1991.

Vaughan, G., Wareing, D. P., Thomas, L., and Mitev, V.: Humidity measurements in the free troposphere using Raman backscatter, Q. J. Roy. Meteor. Soc., 114, 1471–1484, 1988.

Veberic, D.: Maximum-likelihood reconstruction of photon returns from simultaneous analog and photon-counting lidar measurements, Appl. Opt., 51, 139–147, 2012.

Venable, D. D., Whiteman, D. N., Calhoun, M. N., Dirisu, A. O., Connell, R. M., and Landulfo, E.: A Lamp Mapping Technique for Independent Determination of the Water Vapor Mixing Ratio Calibration Factor for a Raman Lidar System, Appl. Opt., 50, 4622–4632, 2011.

Vömel, H., Barnes, J. E., Forno, R. N., Fujiwara, M., Hasebe, F., Iwasaki, S., Kivi, R., Komala, N., Kyrö, E., Leblanc, T., Morel, B., Ogino, S.-Y., Read, W. G., Ryan, S. C., Saraspriya, S., Selkirk, H., Shiotani, M., Valverde Canossa, J., and Whiteman, D. N.: Validation of Aura Microwave Limb Sounder water vapour by balloon-borne Cryogenic Frost point Hygrometer measurements, J. Geophys. Res., 112, DS24S37, doi:10.1029/2007JD008698, 2007.

Ward, J. H.: Hierarchical grouping to optimize an objective function, J. Am. Statist. Assoc., 58, 236–244, 1963.

Whiteman, D. N., Melfi, S. H., and Ferrare, R. A.: Raman lidar system for the measurement of water vapour and aerosols in the Earth's atmosphere, Appl. Opt., 31, 3068–3082, 1992.

Whiteman, D. N., Demoz, B., and Wang, Z.: Subtropical cirrus cloud extinction to backscatter ratios measured by Raman Lidar during CAMEX-3, Geophys. Res. Lett., 31, L12105, doi:10.1029/2004GL020003, 2004.

Whiteman, D. N., Demoz, B., Di Girolamo, P., Comer, J., Veselovskii, I., Evans, K., Wang, Z., Cadirola, M., Rush, K., Schwemmer, G., Gentry, B., Melfi, S. H., Mielke, B., Venable, D., and Van Hove, T.: Raman water vapour lidar measurements

during the International $H_2O$ Project. I. Instrumentation and analysis techniques, J. Atmos. Ocean. Technol. 23, 157–169, 2006.

Whiteman, D. N., Rush, K., Rabenhorst, S., Welch, W., Cadirola, M., McIntire, G., Russo, F., Adam, M., Venable, D., Connell, R., Veselovski, I., Forno, R., Mielke, B., Stein, B., Leblanc, T., McDermid, S., and Vömel, H.: Airborne and Ground-based measurements using a High-Performance Raman Lidar, J. Atmos. Ocean. Technol., 27, 1781–1801, 2010.

Whiteman, D. N., Venable, D., and Landulfo, E.: Comments on: accuracy of Raman lidar water vapour calibration and its applicability to long-term measurements, Appl. Opt., 50, 2170–2176, 2011a.

Whiteman, D. N., Vermeesch, K. C., Oman, L. D., and Weather, E. C.: The relative importance of random error and observation frequency in detecting trends in upper tropospheric water vapour, J. Geophys. Res., 116, D21118, doi:10.1029/2011JD016610, 2011b.